PAPER

Check for updates

The distortion of two FePO$_4$ polymorphs with high pressure†

Craig L. Bull, [iD] *[ab] Christopher J. Ridley, [iD] [a] Nicholas P. Funnell, [iD] [a]
Craig W. Wilson[c] and Simon G. MacLeod[c]

Both the trigonal (Berlinite-type, phase-I), and orthorhombic (CrVO$_4$-type, phase-II) forms of FePO$_4$ have been studied at high-pressure using neutron powder diffraction. Phase-II was prepared by a high-pressure, high-temperature synthetic route, and recovered to ambient conditions. We report the first experimental high-pressure structural study of this phase up to $\sim$8.4 GPa at room temperature. It is shown that with increasing pressure, the FeO$_6$ octahedra become more regular and decrease in volume, while the PO$_4$ tetrahedra become less regular and increase in volume. For phase-I, similar changes in volume are determined, though without changes in distortion. At $\sim$2 GPa a signature of amorphisation has been observed for phase-I with the appearance of broad phase-II reflections. To support the results of the high-pressure study, Raman spectroscopic and SQUID magnetometry studies have been performed.

1 Introduction

The most common polymorph of FePO$_4$, here referred to as phase-I, is iso-structural with Berlinite (AlPO$_4$), with trigonal $P3_121$ symmetry, consisting of a network of corner-shared FeO$_4$ and PO$_4$ tetrahedra as shown in Fig. 1.[1] By the application of pressure and temperature ($\sim$5 GPa at 1170 K) phase-I transforms to phase-II, which is iso-structural with CrVO$_4$, with orthorhombic *Cmcm* symmetry. Phase-II is recoverable to ambient conditions (with a density $\sim$23% higher than phase-I).[2] In phase-II the coordination of Fe^{3+} ions changes from 4 to 6, forming edge-shared chains of FeO$_6$ octahedra along the *c*-axis which are linked *via* corner sharing PO$_4$ tetrahedra (see Fig. 1).

Some applications of FePO$_4$ include use as a catalyst in the manufacture of acrylic composites,[3] oxidation prevention of metals,[4] base coating for improved paint adhesion[5] and as intercalated electrodes in lithium-ion batteries.[6] It also finds an application as an approved pesticide in organic farming.[7]

Mössbauer studies show that phase-I is antiferromagnetic with a Néel temperature of 25 K.[8] This is confirmed by susceptibility and neutron diffraction measurements which also suggested spin-reorientation transition at $\sim$17 K.[9] In contrast, phase-II has a Néel temperature of $\sim$60 K with weak

chain coupling leading to a relaxation phenomena between 43 K and T_N. Phase-I has a resistivity greater than 4×10^{13} Ω cm and phase-II at room temperature is an insulator with a resistivity of 2×10^7 Ω cm.[10]

The physical and structural properties of many ABO$_4$-type oxides have been well studied,[11] these include the orthophosphates, vanadates[12] and quartz-like silicates[13] *e.g.* CrPO$_4$,[14] TiPO$_4$[15] and InPO$_4$.[16] Some of these materials have been studied because they are homeotypes of α-quartz. Varying the cation size changes the level of distortion in the material through chemical means. The use of high-pressures on these homeotypes helps to understand silica polymorphism at less experimentally achievable pressures, to aid our understanding of processes which occur in the Earth's mantle.[17,18] The orthophosphates are of interest, as the structures are intermediate between purely tetrahedral (quartz-like) and purely octahedral coordinated cations. Orthophosphates are predicted to undergo phase transitions to the latter under compression. An example where this has been observed is AlPO$_4$ (pure tetrahedral), which transforms to a highly crystalline CrVO$_4$ structure (mixed tetrahedral/octahedral) under compression and laser annealing. Further compression of this phase at ambient temperature shows a continuous transformation complete by $\sim$75 GPa to a monoclinic distorted CaCl$_2$ structure (pure octahedral).[17]

The room temperature high-pressure behaviour of phase-I has been previously investigated by X-ray diffraction and Raman spectroscopy and found to transform to the orthorhombic phase (phase-II) at around 2.5 GPa. This is accompanied by a significant amount of amorphisation, and upon recovery does

[a] *ISIS Neutron and Muon Facility, Rutherford Appleton Laboratory, Chilton, UK.*
   E-mail: craig.bull@stfc.ac.uk; Tel: +44(0)1235 445706
[b] *School of Chemistry, University of Edinburgh, David Brewster Road,*
   Edinburgh EH9 3FJ, Scotland
[c] *AWE, Aldermaston, Reading, RG7 4PR, UK*

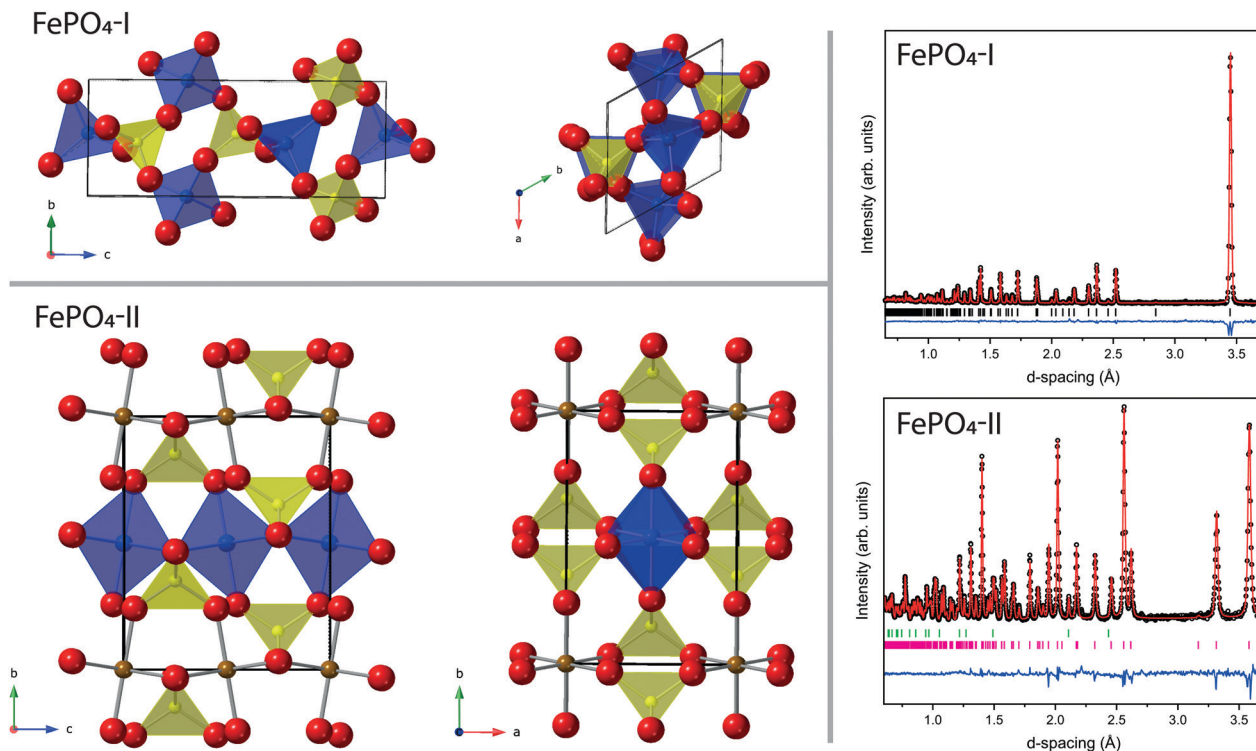**Fig. 1** Top left: Ambient pressure structure of FePO$_4$-I. Bottom left: Ambient pressure structure of FePO$_4$-II. In both structures the yellow and purple polyhedra are the phosphorus and iron polyhedral units respectively and the red spheres the oxygen atoms. The FeO$_6$ octahedra in FePO$_4$-II are only shown in purple for one row along the c-axis, for clarity. The black outline indicates the unit cell. Top right: Ambient pressure neutron diffraction patterns and Rietveld fit for FePO$_4$-I. Bottom right: Ambient pressure neutron diffraction patterns and Rietveld fit for FePO$_4$-II. In both diffraction patterns the open black circles are the measured data, the solid red line is the Rietveld fit, the blue trace is the residual to the fit, the vertical tick marks index reflections to the $P3_121$ for FePO$_4$-I and $Cmcm$ structure for FePO$_4$-II respectively, also shown in the pattern of FePO$_4$-II are the tick marks (in green) for the reflections of the contaminant phase MgO.

not convert back to phase-I but remains a mixture of poorly crystalline phase-II and amorphous FePO$_4$.[19] Such behaviour is similar to that observed in SiO$_2$, which forms an ordered sixfold coordinated structure at 60 GPa.[20] However, the presence of the amorphous material prevented a detailed structural study of phase-II at high pressure. There has also been. theoretical work published on the relative stability of phase I and II.[21]

For the present study, highly crystalline phase-II is instead synthesised and recovered to ambient conditions, as described by Kinomura $et\ al.$[22] This allows the crystallographic changes in the structure of phase-II to be determined starting from ambient pressure up to a pressure of $\sim$8 GPa. In particular we have been able to determine the behaviour of the FeO$_6$ and PO$_4$ polyhedra. To complement this study, we have performed the equivalent diffraction study on phase-I. In addition, Raman scattering and magnetic measurements have been performed to support the work.

2 Experimental

2.1 Synthesis and characterisation

Trigonal phase-I was prepared by mixing stoichiometric amounts of dried Fe$_2$O$_3$ and (NH$_4$)$_2$HPO$_4$. The ground powder was annealed at 1173 K for 24 hours in air.[2] The resulting

material is beige in colour and was confirmed to be pure phase-I by X-ray diffraction (details below). To synthesise phase-II, approximately 200 mg of phase-I was sealed within a platinum capsule and mounted inside a high temperature gasket assembly.[23] The gasket assembly was compressed to $\sim$5 GPa within a V4 Paris-Edinburgh Press[24] and annealed at $\sim$1200 K for 60 minutes. The temperature was decreased to ambient and the sample pressure slowly returned to ambient. The sample was removed from the platinum capsule, and the sample colour had changed to pale green. An X-ray diffraction pattern confirmed the transformation to the orthorhombic $Cmcm$ phase, using a Bruker Phaser D2 with a 2θ range of 15–80° and a step size of 0.01°. The synthesis process was repeated to produce multiple batches, which were all confirmed individually to be single phase, and then combined. A neutron powder diffraction measurement was performed on both phases using the POLARIS instrument at the ISIS Neutron and Muon Source, UK.[25]

2.2 High-pressure neutron diffraction

High-pressure neutron-diffraction measurements were performed on the PEARL instrument at the ISIS Neutron and Muon Source, UK.[26] The sample was loaded into a TiZr null-scattering encapsulated gasket.[27] Phase-I was loaded within a

standard single toroidal setup, and phase-II was loaded into a double toroidal setup, both using zirconia toughened alumina anvils.[28] In both cases, a lead pellet was included with the sample to act as a pressure marker[29] and perdeuterated methanol:ethanol (4:1 by volume) was included as a pressure-transmitting medium.[30] Load was applied to the assemblies using a V3 Paris-Edinburgh press.[24] Time-of-flight (ToF) diffraction patterns were obtained in the transverse geometry and diffraction data were collected for ~ 2 hours per pressure step for phase-I and ~ 8 hours for phase-II. The data were reduced and corrected for anvil attenuation using Mantid.[31] The resulting ToF diffraction patterns were analysed using the GSAS suite of programmes.[32]

2.3 Raman spectroscopy

Raman spectra were obtained in back scattering geometry using a Princeton Instruments SP2500i spectrometer fitted with a 1800 g mm^{-1} holographic blaze grating. A 532 nm diode laser was focused using a 20× Mitutoyo objective with a power of 5 mW at the sample position. All spectra were obtained at room temperature. The Raman measurements obtained at high-pressure were performed in a Almax Nitro membrane driven diamond anvil cell (DAC) equipped with 500 μm culet diamonds, a ruby sphere was included in the sample chamber to act as a pressure calibrant, using the fluorescence method.[33] Methanol:ethanol (4:1) was also included as a pressure transmitting medium.

2.4 Magnetic characterisation

Magnetisation measurements were performed with a Quantum Design MPMS3 SQUID magnetometer in VSM (Vibrating Sample Magnetometry) mode. Finely ground samples (typically ~ 20 mg) were loaded into gelatine capsules, and held in plastic straws within the SQUID at 300 K. Measurements of the DC magnetisation were made as a function of temperature on warming (M vs. T) over the range 4–370 K in an applied field of 100 Oe. Both field-cooled (FC) and zero-field-cooled (ZFC) data were collected.

3 Results

3.1 Ambient pressure structure

The neutron diffraction patterns and associated Rietveld refined fits to the phase-I and phase-II structures are shown in Fig. 1. The results of the refinements of both phases are presented in Table 1. Phase-I is shown to be single phase, and the structure is comparable to that previously published.[34] The sample of phase-II is contaminated with a small quantity of MgO from the gasket assembly and the results of the refinement are in reasonable agreement with previous published data collected by X-ray diffraction.[35]

The work of Baur looked at the distortions of PO_4 tetrahedra in many materials.[36] It was shown that there was a range of P–O bond distances with an average value of 1.537 Å and the tetrahedral angles O–P–O ideally being $\sim 109.5°$. However, the

Table 1 Crystallographic structure and quality of fit information determined from Rietveld refinement of neutron diffraction data to trigonal $FePO_4$-I and orthorhombic $FePO_4$-II structures at ambient pressure and temperature

Parameter	$FePO_4$-I	$FePO_4$-II
Space group	$P3_121$	$Cmcm$
a (Å)	5.03783(7)	5.23106(19)
b (Å)	5.03783(7)	7.7745(3)
c (Å)	11.2498(3)	6.3326(2)
Unit cell volume (Å^3)	247.265(6)	257.540(18)
Fe_x	0.4568(5)	0
Fe_y	0	0
Fe_z	0.33333	0
P_x	0.4570(9)	0
P_y	0	0.3504(2)
P_z	0.83333	0.25
$O(1)_x$	0.4153(7)	0
$O(1)_y$	0.3164(6)	0.24185(13)
$O(1)_z$	0.39594(17)	0.05057(16)
$O(2)_x$	0.4113(8)	0.2437(2)
$O(2)_y$	0.2650(6)	0.46706(13)
$O(2)_z$	0.8752(2)	0.25
wR_P, R_P	3.1,4.4	3.5,4.9
χ^2	3.8	4.9

majority of PO_4 tetrahedra are distorted through variations in P–O bond distances and O–P–O bond angles. Distortions in Fe and P polyhedra can be quantified using distortion indices (DI), defined as

$$DI_{XO} = \frac{1}{n} \sum_{i=1}^{n} \left(XO_i - \overline{XO} \right)$$

where n is the number of bonds (tetrahedral: 4, octahedral: 6), XO_i the individual bond distances within the XO_n polyhedra (where for current study X is Fe or P), and $\overline{XO}$ the mean bond distance within the polyhedron. A value of zero indicates an ideal undistorted polyhedron. The DI for the polyhedra of phases-I- and II at ambient pressure are given in Table 2, showing that the polyhedra in phase-II are more distorted than in phase-I.

3.2 Compressibility of phase-I and -II

Upon compression there are no unexpected changes in the diffraction patterns of phase-I up to ~ 1.7 GPa. However, above this there is a decrease in the intensity of reflections, most apparent in the (102) reflection around 3.37 Å (Fig. 2), with the

Table 2 P–O and Fe–O bond distances of $FePO_4$-I and $FePO_4$-II determined from Rietveld refinement of ambient pressure neutron diffraction measurements. Mean ⟨P–O⟩ and ⟨Fe–O⟩ polyhedral bond distances, also shown are the distortion indices for the polyhedra (DI_{XO})

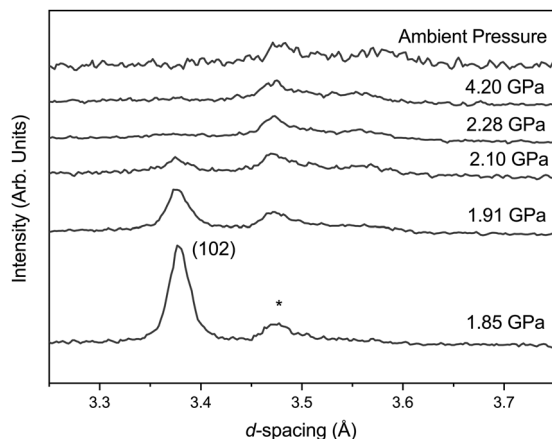| Parameter	$FePO_4$-I	$FePO_4$-II
P–O(1) (Å)	1.534	1.519
P–O(2) (Å)	1.538	1.565
⟨P–O⟩ (Å)	1.536	1.542
DI_{PO}	0.0012	0.0148
Fe–O(1) (Å)	1.848	1.907
Fe–O(2) (Å)	1.857	2.090
⟨Fe–O⟩ (Å)	1.852	2.029
DI_{FeO}	0.0024	0.0401

Fig. 2 Neutron diffraction patterns of FePO$_4$-I with increasing pressure. The reflection at ~ 3.37 Å is the (102) reflection of FePO$_4$-I, the reflection at ~ 3.47 Å is the (asterisk) reflection of the Al$_2$O$_3$ from the anvil and the emerging but broad feature at ~ 3.56 Å can be indexed as the (111) reflection of FePO$_4$-II.

emergence of a new broad feature at ~ 3.56 Å. This broad peak can be approximately indexed as the (111) reflection of the orthorhombic phase-II. The reflections of phase-I disappear completely upon further compression to ~ 2.28 GPa, and the broad (111) reflection of phase-II increases in intensity but remains broad. The intensity and width remain unchanged between ~ 2.28 GPa and 4.2 GPa. Upon recovery to ambient pressure the sample does not revert back to phase-I and the crystallinity does not return.

Diffraction data collected in a vanadium holder on the POLARIS instrument of the recovered sample show broad reflections sitting on an amorphous-like background. The crystalline peaks can be indexed to that of phase-II but not fitted to any acceptable metric by Rietveld refinement techniques as a result of the strained and broad nature of the reflections (see ESI†) suggesting that only phase-II is present albeit strained and poorly crystalline form as indicated by the width of the (111) reflection. The recovered state of the sample is referred to here as phase-Ir.

Prior to the start of the transformation to the strained orthorhombic phase no discontinuous behaviour is observed and the compressibilities of the unit-cell axes are 14.0(4) TPa^{-1} for the a-axis and 6.8(2) TPa^{-1} for the c axis. The variation in unit-cell volume with pressure has been fitted with a 2nd and 3rd order Birch–Murnaghan equation of state (EoS); the fits are shown in the ESI,† and the results given in Table 3. A value of 24 GPa for B$_0$ agrees with that previously reported by Pasternak et al.[19]

In contrast phase-II remains crystalline up to ~ 8 GPa (see Fig. 3) and no changes in crystal symmetry are observed. The determined unit-cell volumes have been fitted with a Birch–Murnaghan EoS and the values are given in Table 3, and no discontinuous behaviour in unit-cell volume is observed. The determined value of bulk modulus (B$_0$) of 104(4) GPa is significantly higher than that determined for phase-I of 24 GPa. However, given that phase-II is 23% higher

Table 3 Compressibility of FePO$_4$. The results of a 2nd and 3rd order Birch–Murnaghan EoS fit are detailed for both phases, V_0 is the derived unit cell volume at ambient pressure, B_0 the bulk modulus and B' the pressure derivative of B_0. Also shown are the median compressibilities (K) of each of the three crystallographic directions as determined using the PASCal program[40]

Phase (BM order)	V_0	B_0	B'
I (2nd)	285.14(11)	25.4(3)	—
I (3rd)	285.28(19)	24.2(12)	5.5(16)
II (2nd)	256.99(10)	111(1)	—
II (3rd)	257.19(14)	104(4)	5.7(10)

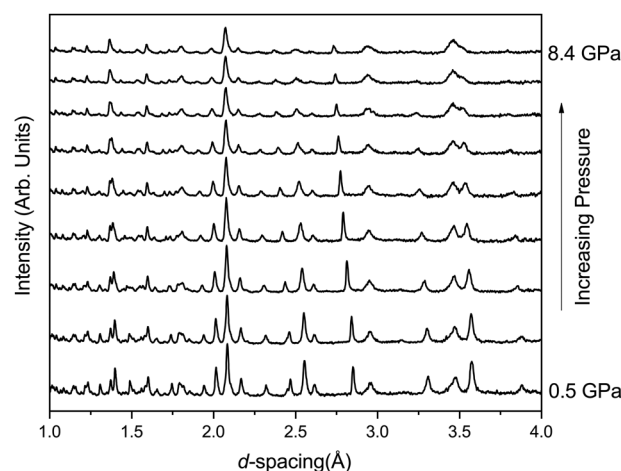|	Median compressibility K (TPa^{-1})		
Phase	a	b	c
I	14.01(39)	14.01(39)	6.75(19)
II	0.97(14)	2.50(17)	3.37(15)

Fig. 3 Neutron diffraction patterns of FePO$_4$-II with increasing pressure.

in density than phase-I this is not surprising.[22] The value is similar to that reported previously by Pasternak et al. of 96 GPa which was determined from a sample formed by compression of phase-I and measured in the presence of the amorphous material and strained phase-II.[19] Other iso-structural Cmcm materials show similar values of B$_0$ for example, 97(6) GPa and 118(7) GPa for InPO$_4$ and AlPO$_4$ respectively.[37,38] Similar increases in B$_0$ are observed in SiO$_2$ when transformed from the α-quartz form to coesite (~ 38.5 GPa to 93 GPa).[39]

Table 3 shows the behaviour of the individual unit-cell axes of phase-II; the c-axis is the least compressible and the a and b-axes are significantly more compressible, with the b-axis slightly stiffer than of the a-axis (see Table 3). The c-axis is the direction in which the chains of FeO$_6$ octahedra are formed explaining the resistance in comparison to the other directions (Fig. 1). Upon compression to 8.4 GPa the angle between the octahedra (O(2)–O(2)′–O(2)″) increases from 162.0(2)° to 175.7(9)°.

3.3 Polyhedral behaviour with pressure

Fig. 4 shows the variation in the FeO$_4$ and PO$_4$ tetrahedra of phase-I up to 1.7 GPa beyond which the phase transition

described above occurs. All of the Fe–O bonds in the tetrahedra decrease in length with increasing pressure, resulting in a decrease in tetrahedral unit volume (see Fig. 4). The bond lengths decrease at a similar rate, so no measurable change in the distortion of the FeO_4 tetrahedra are observed. The PO_4 tetrahedra behave differently, with the longer P–O bonds of the tetrahedra contracting with pressure and the shorter bonds extending. Overall this results in an increase of the tetrahedral unit volume, though still without a measurable change in distortion. This is instead accommodated by a change in angle between the Fe- and P-tetrahedra, which decreases with applied pressure (see Fig. 4).

The behaviour of the octahedral Fe–O bonds in phase-II are shown in Fig. 5 with the longer of the Fe–O bonds decreasing in length whilst the shorter Fe–O bond show very little change with increasing pressure. The longer Fe–O bonds lie in the a–c plane and the shorter Fe–O bonds are tilted off axis along b. The combination of these two opposing bond length changes within the polyhedra result in a decrease in the distortion of the FeO_6 polyhedra as shown by a decrease in the distortion index (DI_{FeO}, Fig. 5).
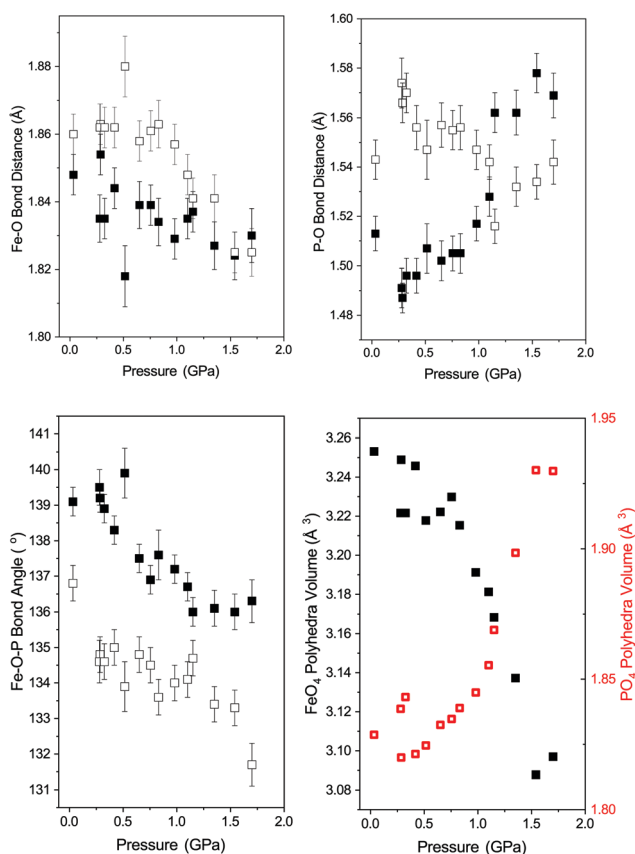
Fig. 4 Polyhedra behaviour in $FePO_4$-I with pressure. Top left: Variation in the distinct Fe–O bond lengths in the FeO_4 tetrahedra (Fe–O(1) filled squares and Fe–O(2) open squares). Top right: Variation in the two distinct P–O bond lengths in the PO_4 tetrahedra (P–O(1) filled squares and P–O(2) open squares). Bottom left: Variation in distinct Fe–O–P bond angles (filled squares – Fe–O(1)–P and open squares –Fe–O(2)–P) between the PO_4 and FeO_4 tetrahedra. Bottom right: Variation in volume of the PO_4 (open red squares) and FeO_4 tetrahedra (filled black squares).
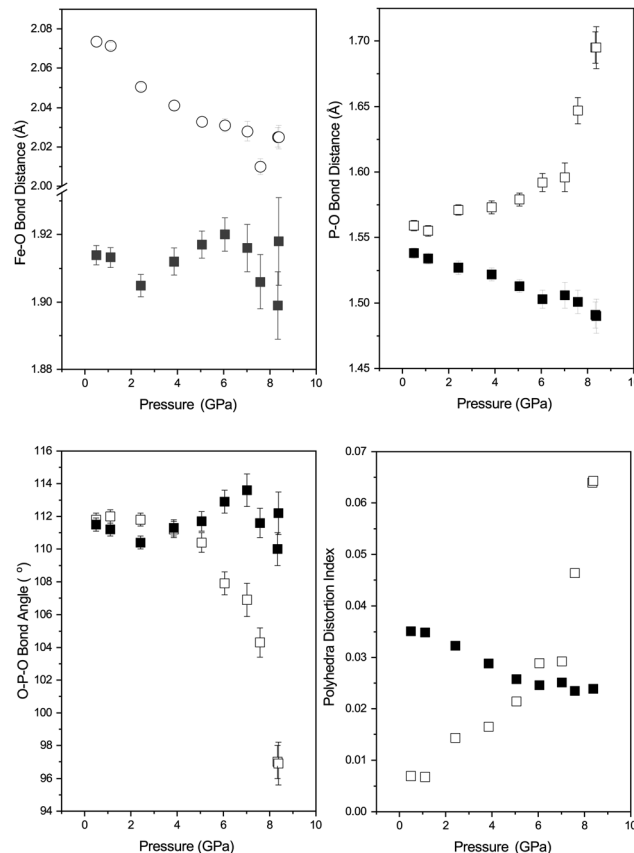
Fig. 5 Polyhedra behaviour of $FePO_4$-II with pressure. Top left: Variation in Fe–O bond lengths in the FeO_6 octahedra (Filled squares – Fe–O(1) and open squares Fe–O(2)). Top right: Variation in P–O bond lengths in PO_4 tetrahedra (Filled squares – P–O(1) and open squares P–O(2)). Bottom left: Variation in O–P–O bond angles (solid squares – O(1)–P–O(1) and the filled squares O(2)–P–O(2)) in the PO_4 tetrahedra. Bottom right: Variation in the distortion indices (DI_{PO}) for the PO_4 tetrahedra (open squares) and FeO_6 octahedra (DI_{FeO}) shown by filled squares.

The behaviour of the bond lengths in the PO_4 tetrahedra of phase-II are shown in Fig. 5. At ambient pressure the two distinct P–O bond lengths are similar, however, with increasing pressure the P–O(1) bonds decrease in length and the longer P–O(2) bonds show a significant increase in length. Similarly, the O(1)–P–O(1) and O(1)–P–O(2) bond angles show very little variation within experimental error, however, the O(2)–P–O(2) bond angle shows a significant pressure dependence and a decrease away from the ideal tetrahedral value of 109.5°. The distortion indices (DI_{PO}) for the PO_4 tetrahedra show an increase with compression in contrast to that seen for the FeO_6 octahedra. This is different to the behaviour of the isostructural $CrVO_4$ structured $InPO_4$ at high pressure.[37] Upon compression of orthorhombic $InPO_4$ both of the P–O bonds in the PO_4 tetrahedra decrease in length at a similar rate to each other, and both of the O–P–O angles increase, resulting in no change in overall distortion of the tetrahedral unit with increasing pressure.

In the compression study of $AlPO_4$ the transition from the orthorhombic phase to a monoclinic phase is observed in
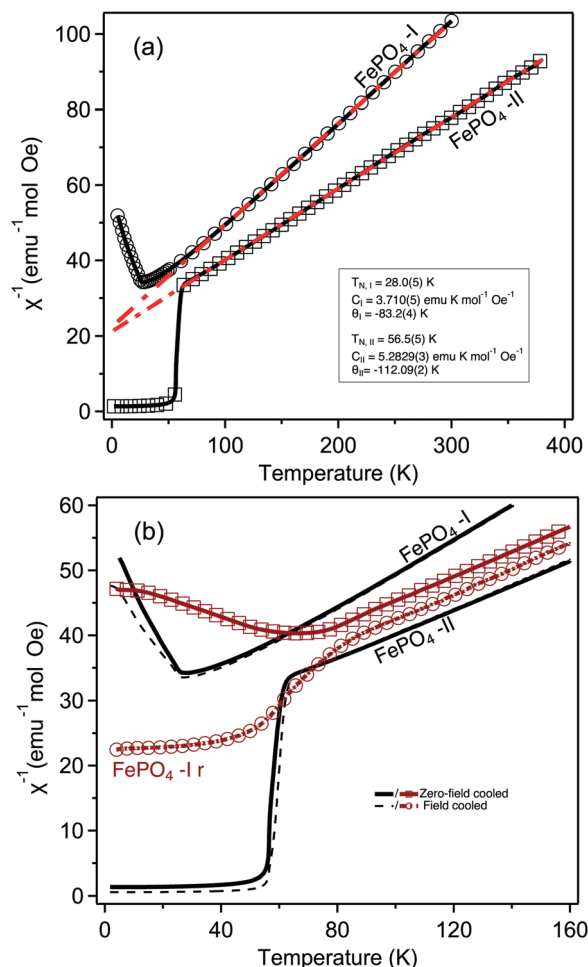

Fig. 7 Temperature dependence of magnetic susceptibility of $FePO_4$. (a) ZFC inverse susceptibility of the two phases of $FePO_4$ at ambient pressure, fitted to Curie–Weiss law (red dashed line, see text). (b) ZFC (solid/squares) and FC (dashed/circles) inverse susceptibilities of both phases at ambient pressure, compared with that of the recovered sample ($FePO_4$-Ir) from 4.2 GPa (red squares and circles) below T_N.

complexes to be high-spin. For d^5-complexes this means that the theoretical spin-only effective moment is identical as that for octahedral coordination. An alternative cause for a lower effective moment, may be an oxygen deficiency, resulting in a proportion of Fe^{2+} in the sample. Refining the two site occupancies against the ambient neutron-diffraction data gives values of 0.97(1) and 0.96(1). This would average to give $Fe^{2.7+}$, still not completely accounting for the measured value being lower than expected. Alternatively, there could be a mixture of high- and low-spin Fe^{3+}, though this would have been evident in the isomer shift in previous Mössbauer studies, which appear consistent with a high-spin arrangement. It is therefore likely that some undetectable (*via* neutron diffraction) level of impurity in the precursor material exists.

No anomalies are observed in the susceptibility of phase-I at ~17 K as initially reported by Battle *et al.*,[9] and confirmed more recently by Grandjean *et al.* with Mössbauer, attributed to an antiferromagnetic spin reorientation, which may be due to differences in measuring field (see ESI†).[49]

Phase-Ir, shows very different magnetisation behaviour from both phase-I and phase-II. While the Néel temperature for phase-II is greater than phase-I, it is greater still for phase-Ir, 66(2) K. Additionally there is a clear split in the FC and ZFC datasets, which is not observed to the same level in either phase-I or phase-II. This suggests that there is a significant degree of uncompensated moment in the antiferromagnetic state. This type of behaviour may be attributed to a number of phenomena, such as super-paramagnetism (as is observed with $DyPO_4$[50]), domain wall pinning, clustering, or spin-glass behaviour. Literature measurements on amorphous $MnPO_4$, obtained by delithiation of $LiMnPO_4$, and annealing at 970 K in O_2 atmosphere, showed a similar large discrepancy in FC/ZFC curves, though the authors suggest that an impurity phase may be the cause of this.[51] In the present study, this spin canting may be due to a highly strained frustrated intermediate state between phase-I and -II, which is supported by the evidence for reduced crystallinity in the diffraction data. Similar effects are seen in $CoPO_4$ units when frustrated through layering in the compound $Ba(CoPO_4)_2$.[52] Further time dependent, and AC measurements would be required to aid differentiating between these possibilities, which are beyond the scope of the present study.

4 Conclusions

We have for the first time followed the structural behaviour of both the trigonal and orthorhombic phases of $FePO_4$ as a function of pressure at room temperature using neutron diffraction. With increasing pressure the FeO_4 and PO_4 tetrahedra of phase-I show no significant change in distortion however, the FeO_4 units decrease in volume and the PO_4 tetrahedra increase in volume. At ~1.8 GPa phase-I appears to partially amorphise, concurrent with the appearance of the orthorhombic phase-II with broad reflections indicating a highly strained state. This state is recoverable when the pressure is reduced back to ambient conditions. Raman measurements on the recovered sample show properties similar to that of pure phase-II, while SQUID data shows a large increase in T_N, and large uncompensated moment in the antiferromagnetic state. In contrast to the behaviour of phase-I, the PO_4 tetrahedra in phase-II increase in volume and increase in distortion with pressure, and the FeO_6 octahedra show a decrease in volume and a small decrease in distortion from regular octahedra. The behaviour described of both the trigonal and orthorhombic phases of $FePO_4$ could have implications for geological isostructural materials. Structural studies of many geologically relevant materials may not be achievable using neutron diffraction techniques as a result of the higher pressures required to induce such structural transformations, and the behaviour observed in $FePO_4$ can be used to extrapolate behaviour in minerals. Studies at higher pressures may also be limited by the degree of resolution required to determine accurate crystallographic information at these extremes.

Conflicts of interest

There are no conflicts to declare.

Acknowledgements

References

1 H. N. Ng and C. Calvo, *Can. J. Chem.*, 1975, **53**, 2064–2067.

2 P. Battle, C. Gibb, G. Hu, D. Munro and J. Attfield, *J. Solid State Chem.*, 1986, **65**, 343–350.

3 M. Gadgil and S. Kulshreshtha, *J. Solid State Chem.*, 1994, **111**, 357–364.

4 B. Ptacek, F. Dalard and J. Rameau, *Surf. Coat. Technol.*, 1996, **82**, 277–283.

5 S.-J. Lee, D. Hung-Toan, Y.-H. Chena and H.-C. Peng, *Int. J. Electrochem. Soc.*, 2016, **11**, 2306–2316.

6 A. K. Padhi, *J. Electrochem. Soc.*, 1997, **144**, 1188.

7 S. Freitag, E. M. Krupp, A. Raab and J. Feldmann, *Environ. Sci.: Processes Impacts*, 2013, **15**, 463–469.

8 W. Bruckner, W. Fuchs and G. Ritter, *Phys. Lett. A*, 1967, **26**, 32–33.

9 P. D. Battle, A. K. Cheetham, C. Gleitzer, W. T. A. Harrison, G. J. Long and G. Longworth, *J. Phys. C: Solid State Phys.*, 1982, **15**, L919–L924.

10 M. E. Arroyo y de Dompablo, N. Biskup, J. M. Gallardo-Amores, E. Moran, H. Ehrenberg and U. Amador, *Chem. Mater.*, 2010, **22**, 994–1001.

11 E. J. Baran, *J. Mater. Sci.*, 1998, **33**, 2479–2497.

12 S. López-Moreno and D. Errandonea, *Phys. Rev. B: Condens. Matter Mater. Phys.*, 2012, **86**, 104112.

13 L. Gracia, A. Beltrán and D. Errandonea, *Phys. Rev. B: Condens. Matter Mater. Phys.*, 2009, **80**, 094105.

14 M. Touboul and K. Melghit, *J. Mater. Chem.*, 1995, **5**, 147–150.

15 N. Kinomura, F. Muto and M. Koizumi, *J. Solid State Chem.*, 1982, **45**, 252–258.

16 R. C. L. Mooney, *Acta Crystallogr.*, 1956, **9**, 113–117.

17 J. Pellicer-Porres, A. M. Saitta, A. Polian, J. P. Itié and M. Hanfland, *Nat. Mater.*, 2007, **6**, 698–702.

18 J. Haines and O. Cambon, *Z. Kristallogr. – Cryst. Mater.*, 2004, **219**, 314–323.

19 M. P. Pasternak, G. K. Rozenberg, A. P. Milner, M. Amanowicz, T. Zhou, U. Schwarz, K. Syassen, R. Dean Taylor, M. Hanfland and K. Brister, *Phys. Rev. Lett.*, 1997, **79**, 4409–4412.

20 S. M. Sharma and S. Sikka, *Prog. Mater. Sci.*, 1996, **40**, 1–77.

21 N. Lethole, H. Chauke and P. Ngoepe, *Comput. Theor. Chem.*, 2019, **1155**, 67–74.

22 N. Kinomura, M. Shimada, M. Koizumi and S. Kume, *Mater. Res. Bull.*, 1976, **11**, 457–460.

23 Y. Le Godec, M. T. Dove, D. J. Francis, S. C. Kohn, W. G. Marshall, A. R. Pawley, G. D. Price, S. A. T. Redfern, N. Rhodes, N. L. Ross, P. F. Schofield, E. Schooneveld, G. Syfosse, M. G. Tucker and M. D. Welch, *Mineral. Mag.*, 2001, **65**, 737–748.

24 J. M. Besson, R. J. Nelmes, G. Hamel, J. S. Loveday, G. Weill and S. Hull, *Phys. B*, 1992, **180**, 907–910.

25 R. I. Smith, S. Hull, M. G. Tucker, H. Y. Playford, D. J. McPhail, S. P. Waller and S. T. Norberg, *Rev. Sci. Instrum.*, 2019, **90**, 115101.

26 C. L. Bull, N. P. Funnell, M. G. Tucker, S. Hull, D. J. Francis and W. G. Marshall, *High Press. Res.*, 2016, **36**, 493–511.

27 W. G. Marshall and D. J. Francis, *J. Appl. Crystallogr.*, 2002, **35**, 122–125.

28 P. F. Funnell, C. J. Ridley and C. L. Bull, *In preparation*.

29 A. D. Fortes, RAL Technical Reports, 2019, RAL-TR-2019-002.

30 S. Klotz, J. C. Chervin, P. Munsch and G. L. Marchand, *J. Phys. D: Appl. Phys.*, 2009, **42**, 075413.

31 O. Arnold, J. C. Bilheux, J. M. Borreguero, A. Buts, S. I. Campbell, L. Chapon, M. Doucet, N. Draper, R. Ferraz Leal, M. A. Gigg, V. E. Lynch, A. Markvardsen, D. J. Mikkelson, R. L. Mikkelson, R. Miller, K. Palmen, P. Parker, G. Passos, T. G. Perring, P. F. Peterson, S. Ren, M. A. Reuter, A. T. Savici, J. W. Taylor, R. J. Taylor, R. Tolchenov, W. Zhou and J. Zikovsky, *Nucl. Instrum. Methods Phys. Res., Sect. A*, 2014, **764**, 156–166.

32 B. H. Toby, *J. Appl. Crystallogr.*, 2001, **34**, 210–213.

33 K. Syassen, *High Press. Res.*, 2008, **28**, 75.

34 J. Haines, O. Cambon and S. Hull, *Z. Kristallogr.*, 2003, **218**, 193.

35 M. E. Arroyo-de Dompablo, J. M. Gallardo-Amores and U. Amador, *Electrochem. Solid-State Lett.*, 2005, **8**, A564.

36 W. H. Baur, *Acta Crystallogr., Sect. B: Struct. Sci.*, 1974, **30**, 1195–1215.

37 A. Dwivedi, R. Kaiwart, M. Varma, S. Velaga and H. Poswal, *J. Solid State Chem.*, 2020, **282**, 121065.

38 H. K. Poswal, N. Garg, M. Somayazulu and S. M. Sharma, *Am. Mineral.*, 2013, **98**, 285–291.

39 H. Mao, B. Sundman, Z. Wang and S. Saxena, *J. Alloys Compd.*, 2001, **327**, 253–262.

40 M. J. Cliffe and A. L. Goodwin, *J. Appl. Crystallogr.*, 2012, **45**, 1321–1329.

41 J. S. Tse and D. D. Klug, *Science*, 1992, **255**, 1559–1561.

42 M. Bykov, E. Bykova, M. Hanfland, H.-P. Liermann, R. K. Kremer, R. Glaum, L. Dubrovinsky and S. van Smaalen, *Angew. Chem., Int. Ed.*, 2016, **55**, 15053–15057.

43 D. Errandonea and F. J. Manjón, *Prog. Mater. Sci.*, 2008, **53**, 711–773.

44 M. Souleiman, P. Hermet, A. Haidoux, C. Levelut, J. Haines and O. Cambon, *RSC Adv.*, 2013, **3**, 22078–22086.

45 M. Rokita, M. Handke and W. Mozgawa, *J. Mol. Struct.*, 2000, **555**, 351–356.

46 C. M. Julien, A. Ait-Salah, A. Mauger and F. Gendron, *Ionics*, 2006, **12**, 21–32.

47 R. P. Santoro and R. E. Newnham, *Acta Crystallogr.*, 1967, **22**, 344–347.

48 I. Bobrikov, A. Balagurov, C.-W. Hu, C.-H. Lee, T.-Y. Chen, S. Deleg and D. Balagurov, *J. Power Sources*, 2014, **258**, 356–364.

49 F. Grandjean and G. J. Long, *Inorg. Chem.*, 2019, **58**, 13314–13322.

50 T. Sorop, M. Evangelisti, M. Haase and L. de Jongh, *J. Magn. Magn. Mater.*, 2004, **272-276**, 1573–1574.

51 Y. Huang, J. Fang, F. Omenya, M. O'Shea, N. A. Chernova, R. Zhang, Q. Wang, N. F. Quackenbush, L. F. J. Piper, D. O. Scanlon and M. S. Whittingham, *J. Mater. Chem. A*, 2014, **2**, 12827–12834.

52 R. David, H. Kabbour, A. Pautrat and O. Mentré, *Inorg. Chem.*, 2013, **52**, 8732–8737.

53 C. L. Bull, C. J. Ridley, N. P. Funnell, C. Wilson and S. MacCleod, *STFC ISIS Neutron and Muon Source*, 2019, DOI: 10.5286/ISIS.E.RB2000049-1.

54 C. L. Bull, C. J. Ridley and N. P. Funnell, *STFC ISIS Neutron and Muon Source*, 2020, DOI: 10.5286/ISIS.E.RB2090075-1.

55 C. L. Bull, C. J. Ridley and N. P. Funnell, *STFC ISIS Neutron and Muon Source*, 2019, DOI: 10.5286/ISIS.E.RB1990184-1.

56 C. L. Bull, C. J. Ridley and N. P. Funnell, *STFC ISIS Neutron and Muon Source*, 2019, DOI: 10.5286/ISIS.E.RB1990183-1.